Supporting Information

Zinc Oxoclusters for Extreme Ultraviolet Lithography

Neha Thakur

3

ZINC-BASED OXOCLUSTER: CHEMISTRY FOR HIGH RESOLUTION NANOLITHOGRAPHY*

*Published as: N. Thakur, R. Bliem, I. Mochi, M. Vockenhuber, Y. Ekinci, and S. Castellanos, Journal of Materials Chemistry C, 2020, 8(41), 14499-14506. DOI: 10.1039/D0TC03597A.

1. Images of L/S features patterned with EUV interference lithography

AFM images were recorded with a Bruker Dimensions Icon in ScanAsyst-air mode using a silicon tip on nitride lever of SCANASYST-AIR model (Bruker). Processing of the L/S contours profiles were done using NanoScope Analysis version 2.00 software.

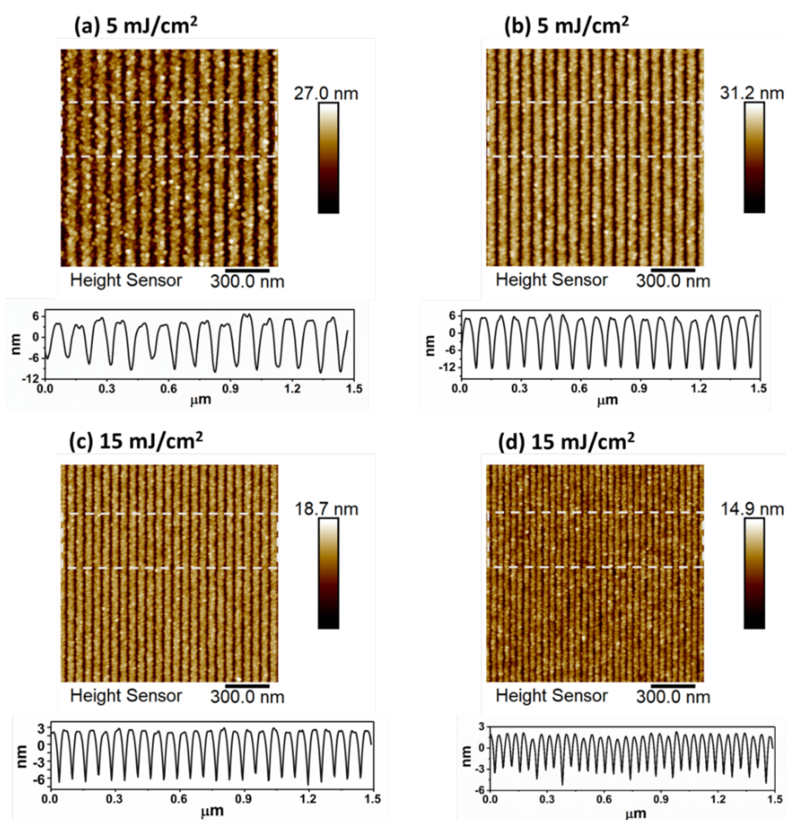

Figure S3.1: Selected AFM images and contour profiles of printed L/S patterns for HP (a) 50 nm, (b) 40 nm, (c) 30 nm, and (d) 22 nm patterned on Zn(MA)(TFA) thin film using EUV-IL.

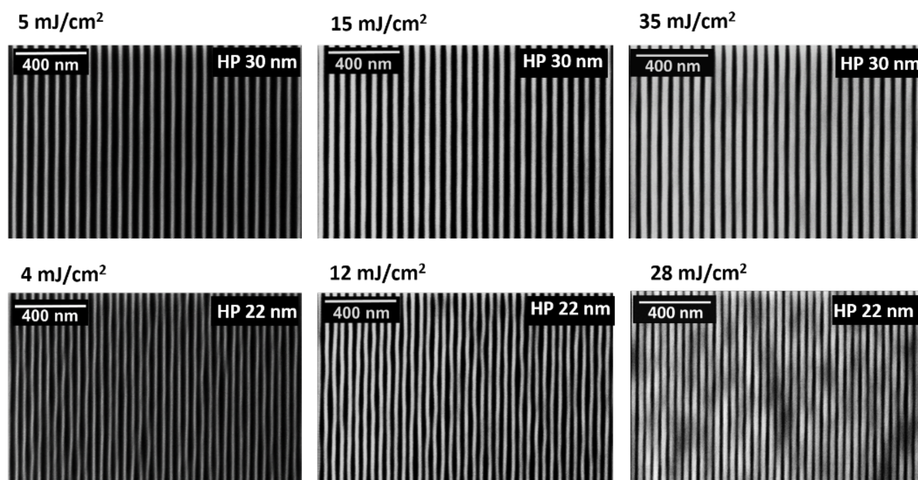

Figure S3.2: Selected SEM (operated at 2 kV) images for HP 30 nm and 22 nm used to calculate the linewidth/ critical dimensions of line/space features over a range of the exposure doses.

2. Control experiments for aging effect

The effect of aging during the time lapse between exposure in the synchrotron facilities and the spectroscopic analyses in our laboratories was inspected by comparing the FTIR and UV-vis spectra of a freshly spin-coated film. A certain degree of cross-linking and decarboxylation is observed, as previously reported.[1] The effect of aging does not eclipse the changes induced by EUV light, which are clearly distinguished.

We concluded from the spectroscopy results that aging has a stronger effect on the MA ligands of the unexposed material than in the exposed one. We hypothesize that, after EUV exposure, the product consists of a more stable cross linked network.

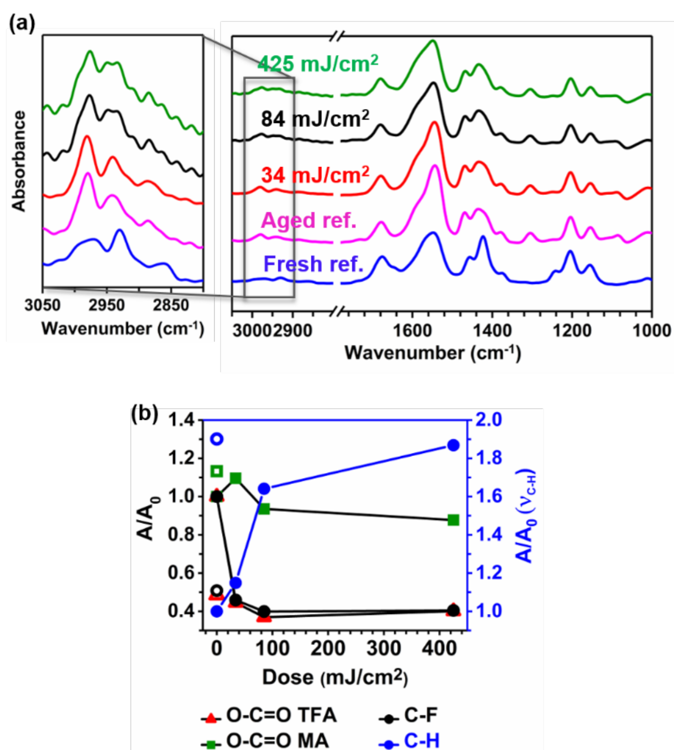

Figure S3.3: (a) FTIR spectra of the exposed (doses given in the graph) and unexposed areas (reference aged) in the sample exposed to EUV and of a freshly spin-coated film (fresh reference), and (b) Peak area ratio of relevant peaks relative to the fresh reference for the exposed areas. The peak area ratio of the aged unexposed area relative to the freshly spin-coated sample is given as hollow markers.

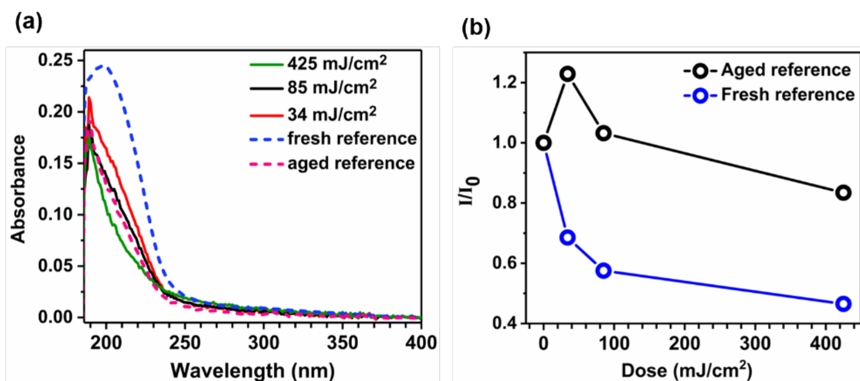

Figure S3.4: (a) UV-vis absorption spectra of the resist film, and (b) change in the UV-vis absorbance maximum relative to the aged and fresh sample as a function of EUV dose.

3. X-ray Photoelectron spectroscopy

No significant changes in the Zn 2*p* region are observed upon the formation of Zn-F species. However, the difference in the BE of Zn 2*p* between a Zn^{2+} with only Zn-O bonds and with Zn-F bonds is less than 1 eV, according to the literature.[2] Here, the concentration of the proposed Zn-F species in the overall Zn-content is estimated to be very low (ca. 15%). This might explain why no changes are observed in the Zn 2*p* peaks.

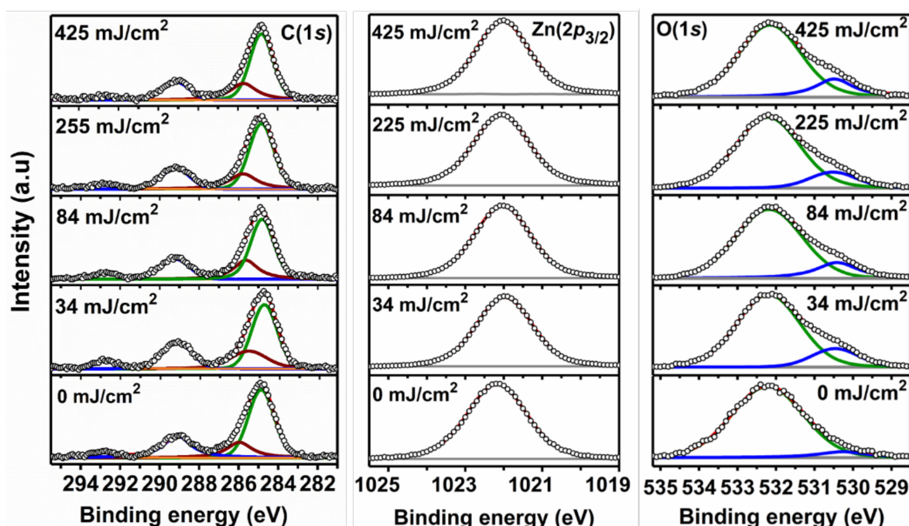

Figure. S3.5: High-resolution spectra of C 1*s*, Zn $2p_{3/2}$, and O 1*s*.

To obtain the information for zinc metal high resolution spectra for $ZnL_3M_{45}M_{45}$ Auger electron spectra were recorded. The separation between these two peaks for both samples fresh and exposed sample (425 mJ/cm^2) was quite constant, 3.1 $\pm$ 0.1 eV.

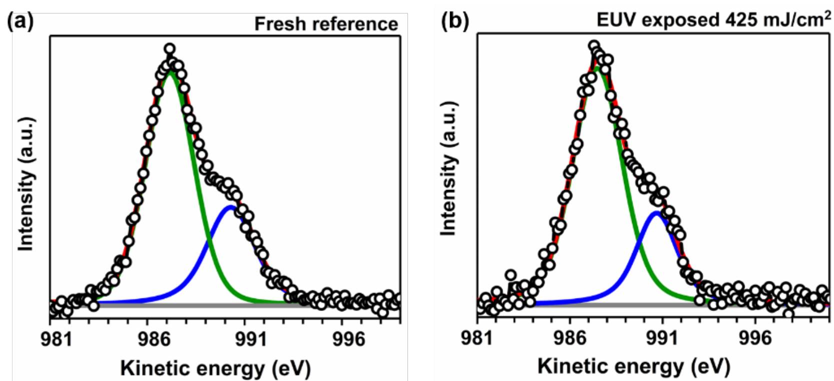

Figure S3.6: High-resolution Zn Auger spectra for unexposed and exposed sample at 425 mJ/cm2. Solid lines without dots represents the fitting results.

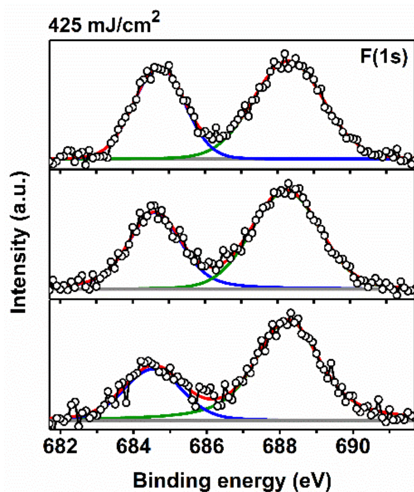

Figure S3.7: From bottom to top: chemical changes induced by X-rays of XPS after consecutive measurements on the sample spot on Zn(MA)(TFA) thin film.

5

ROLE OF ELECTRONS IN THE SOLUBILITY SWITCH OF ZINC OXOCLUSTER†

---

†Published as: M. Rohdenburg, N. Thakur, R. Cartaya, S. Castellanos, and P. Swiderek, Physical Chemistry Chemical Physics, 2021, 23(31), 16646-16657. DOI: 10.1039/D1CP02334A.

1. Estimate of relative product amounts in ESD

The relative amounts of the desorbing products as compared to CO_2 can be roughly estimated based on the intensities in the ESD data (Figure 5.2). This estimate requires: (i) a unique assignment of the particular signals in the mass spectrum (MS) resulting from ESD to specific products, (ii) absolute ionization cross sections for these products at 70 eV, i.e., the energy used in the QMS, and (iii) knowledge of the fragmentation pattern of these products following ionization, i.e., of the MS.[3–5] On top of this, the mass discrimination of the quadrupole mass spectrometer (QMS) used in the present experiments must be taken into account. This residual gas analyser is tuned to enhance, in particular, low m/z ratios. Figure S5.1 thus shows a comparison between the intensity distribution of signals obtained with the present QMS and the MS from the NIST database for n-octane as an example of a compound that exhibits signals in the m/z range relevant to the present study. The spectra are normalized to the signal at m/z 43 which is the strongest signal in the NIST spectrum and closest to the m/z 44 peak of CO_2 to which other desorbing species are compared when the ESD yields from Zn oxoclusters are analysed. Table S5.1 summarizes correction factors for the intensities of specific m/z ratios that must be applied to compare the QMS data to MS data from NIST.

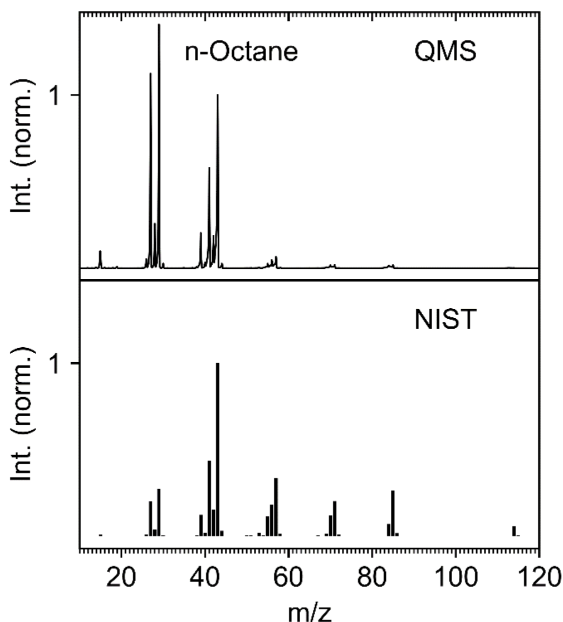

Figure S5.1: MS of n-octane (C_8H_{18}) measured with the QMS used in this study (top) and from the NIST database.[6] Both spectra are normalized to the m/z 43 signal. The comparison reveals that the QMS used in the present experiments discriminates higher masses in favour of lower ones.

The total ionization cross section of CO_2 and the partial ionization cross section for the parent ion at m/z 44 have been reported as 3.27 Å^2 and 2.13 Å^2.[7] Similarly, the total ionization cross section of H_2O is 1.99 Å^2 of which 1.27 Å^2 contribute as the partial ionization cross section for the parent ion at m/z 18.[7] Using these partial cross sections and considering that the contribution of other products to the signals at m/z 44 (CO_2) and m/z 18 (H_2O) is negligible, the relative amounts of H_2O and CO_2 that desorb during electron exposure from Zn(TFA) is derived from the relative peak heights in Figure 5.2(a) as roughly 1:4. However, based on the mass discrimination effect of the QMS (see m/z 15 as closest signal in Figure S5.1 and Table S5.1), this must be corrected to roughly 1:30. A similar result can be derived from Figure 5.2(b) for Zn(MA)(TFA).

The partial ionization cross section for the parent ion of the CF_3 radical has been reported as 0.376 Å^2 [8] and the partial ionization cross section for formation of CF_3^+ from CHF_3 as 0.813 Å^2.[9] Considering also mass discrimination, we deduce from the height of the m/z 69 signal in the case of Zn(TFA) as compared to m/z 44 (CO_2) (Figure 5.2(a)) values of 1:5 (CF_3:CO_2) and 1:10 (CHF_3:CO_2) as an upper and lower limit for the relative yields of desorbing fluorinated products as compared to CO_2.

Table S5.1: Comparison of intensities for selected m/z signals in the MS of n-octane as obtained with the QMS used in this work to MS data retrieved from the NIST database.[6] The spectra are normalized to the m/z 43 signal.

m/z	Relative intensity obtained using QMS	Relative intensity according to NIST	Mass discrimination
15	9	0.9	10
29	138	27.4	5
41	57	43.8	1.3
43	100	100	1
57	7	33.5	0.2
70	2	12.1	0.17

A partial ionization cross section for propene is used to estimate the amount of hydrocarbon products that desorb from the Zn(MA)(TFA) resist under electron irradiation (Figure 5.2(b)). Based on a total ionization cross section of 8.736 Å^2 and the relative intensities in the mass spectrum of propene,[8] we deduce a partial ionization cross section of 2.18 Å^2 for the dominant m/z 41 ($C_3H_5^{\cdot +}$) fragment of propene. From this we arrive at a relative yield of desorbing propene as compared to CO_2 of 1:50 (propene:CO_2).

Table S5.2: Estimate of relative product amount in ESD of Fig. 2 from representative peak heights using partial ionization cross sections (ics) reported in literature or derived as explained in text and including effect of mass discrimination.

	Zn(TFA), Zn(MA)(TFA)	**Zn(TFA)**			**Zn(MA)(TFA)**	
	$CO_2^{+\bullet}$/ CO_2	$H_2O^{+\bullet}$/ H_2O	$CF_3^{+\bullet}$/ CF_3	$CF_3^{+\bullet}$/ CHF_3	$H_2O^{+\bullet}$/ H_2O	$C_3H_5^{+\bullet}$/ $CH_3CH=CH_2$
m/z	44	18	69	69	18	41
Relative Int.	100	19.4	0.65	0.65	15.7	2.5
Partial ics	2.13 Å^2 [7]	1.27 Å^2 [7]	0.376 Å^2 [8]	0.813 Å^2 [9]	1.27 Å^2 [7]	2.18 Å^2 [6,10]
Relative Int./ partial ics/ Å^2	46.9	15.3[a]	1.7	0.8	12.4[a]	1.1
Mass discrimin. factor[b]	1	9	0.17	0.17	9	1.4
Relative amount	100	3.6	21	10	2.9	1.7

a Value to be considered as lower limit because ESD of H_2O decays more slowly than for other species.

b Estimated by interpolation between m/z values listed in Table S5.1.

2. Comparison of ESD of CO_2 at 80 eV and 20 eV

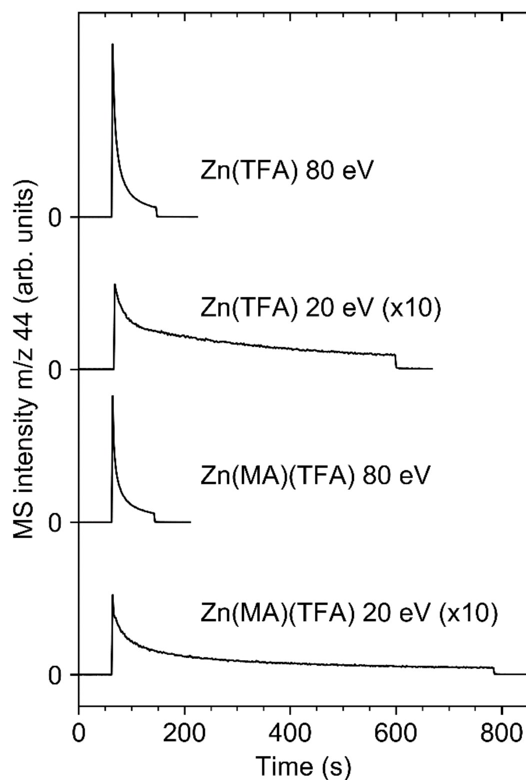

Figure S5.2: . Electron-stimulated desorption (ESD) of CO_2 from 14 nm Zn(TFA) resist layers and from 12 nm Zn(MA)(TFA) resist layers during an electron exposure of 2.5 mC/cm^2 at 80 eV and 20 eV. The sudden drop of the signal marks the end of irradiation. Sample currents during electron irradiation and integrated ESD intensities in arbitrary units (from top to bottom): 30 µA/cm^2 (area 3.39), 4.5 µA/cm^2 (area 1.89), 34.2 µA/cm^2 (area 2.41), 3.9 µA/cm^2 (area 1.33).

3. Vibrational bands of Zn(TFA) and Zn(MA)(TFA)

Table S5.3: Vibrational band positions (in cm^{-1}) observed in RAIRS of Zn(TFA) and Zn(MA)(TFA) resist layers and assignments.

Assignment	Zn(TFA)	Zn(MA)(TFA)	References
ν_{as}(TFA,CO_2)	1683	1682	[1,11]
ν (C=C)		1646	[1,12]
ν_{as}(MA,CO_2)		1595, 1569	[1,12]
ν_s(TFA,CO_2)	1456	1460	[1,11]
ν_s(MA,CO_2)+ δ(CH_2)+ δ(CH_3)		1427, 1375	[12]
ν(C-C)+ρ(=CH_2)		1244	[1,12]
ν_s(CF_3)	1223	1210	[1,11]
ν_{as}(CF_3)	1168	1156	[1,11]
ν(CH_3)		1009	[12]
ν(CH_2)		944	[12]
ν(TFA,CC)	853	850	[11]
CH_2 bending mode		825	[13]
ν (TFA,CO_2)	799	799	[11]
$\nu_{umbrella}$(CF_3)	735	729	[11]

4. RAIRS of Zn(TFA) and Zn(MA)(TFA) before and after electron irradiation

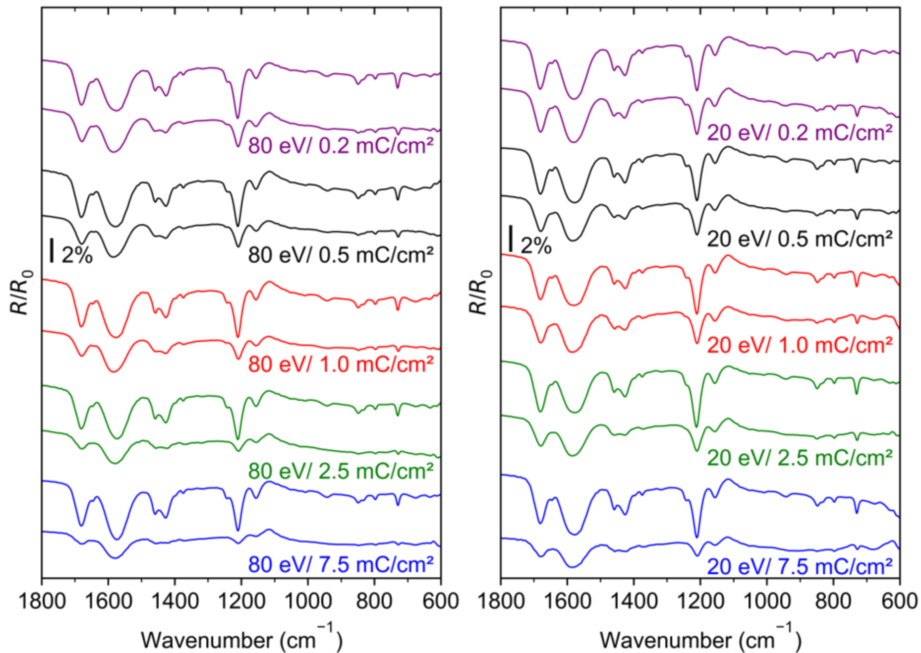

Figure S5.3: RAIRS of 12 nm Zn(MA)(TFA) resist layers before (upper spectrum of each set) and after the stated electron exposures at 80 eV (left) and 20 eV (right).

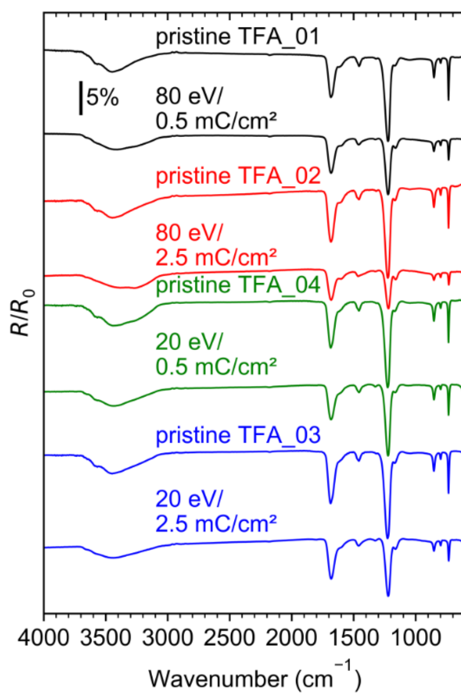

Figure S5.4**:** RAIRS of 14 nm Zn(TFA) resist layers before (upper spectrum of each set) and after the stated electron exposures at 80 eV (top) and 20 eV (bottom).

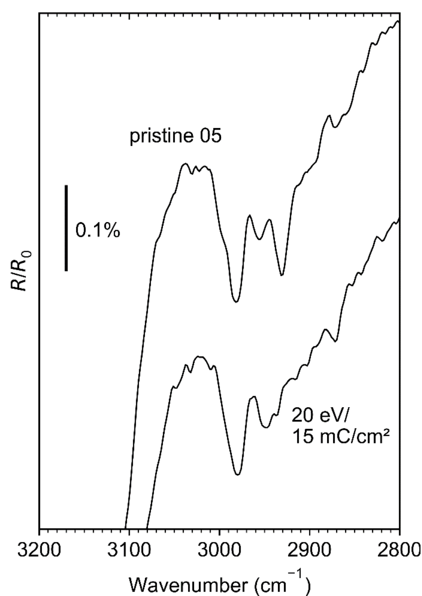

Figure S5.5: C-H stretching spectral range of a 15nm Zn(MA)(TFA) resist layer before and after a 15 mC/cm^2 electron irradiation at 20 eV. Note that the bands are weak and sit on a background caused by formation of ice on the infrared detector thus ruling out their quantitative evaluation.

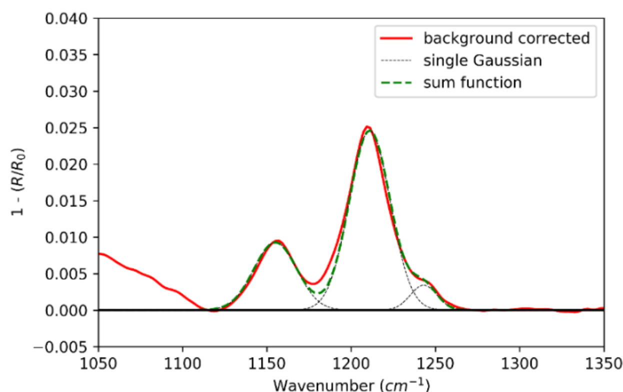

Figure S5.6: Example of a fit of Gaussian functions to the characteristic TFA RAIRS bands $\nu_s(CF_3)$ (1223 cm^{-1}) and $\nu_{as}(CF_3)$ (1168 cm^{-1}) which, by integration of the Gaussians, together yields the overall ν(C-F) intensity as plotted in Fig. 7 of the main text. Equally shown here is the fit to the characteristic MA RAIRS band ν(C-C)+ρ(=CH_2) (1244 cm^{-1}).

6

FLUORINE-RICH ZINC OXOCLUSTER AS EUV PHOTORESIST‡

---

‡Published as: N. Thakur, M. Vockenhuber, Y. Ekinci, B. Watts, A. Giglia, N. Mahne, S. Nannarone, S. Castellanos, and A.M. Brouwer, ACS Materials Au, 2022. DOI: 10.1021/acsmaterialsau.1c00059.

1. Synthesis of Zn(TFMA):

Oxo[hexa(trifluoroacetato)] tetrazinc trifluoracetic acid adduct (Zn(TFA); 500 mg, 0.52 mmol, 1 eq.) and 2-(trifluoromethyl)acrylic acid (TFMAA; 870 mg, 6.2 mmol, 12 eq.) were dissolved in the acetonitrile (solvent) and left for stirring for 5 hours at 45°C. The remaining solvent was then evaporated using rotary evaporator and an oily residue was obtained. The oily residue was then precipitated by adding toluene to the residue and evaporating it on a rotary evaporator. The process was repeated for about 4-5 times to remove access of the reaming acid and obtain a white solid product. The white solid product was dried in the vacuum oven at 40°C and stored under nitrogen conditions.

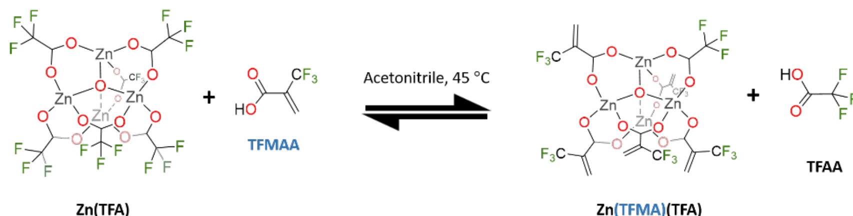

Figure S6.1: Schematic representing the synthesis of $Zn(TFMA)_{5.9}(TFA)_{0.1}$ oxocluster. Labelled as Zn(TFMA) for clarity in the text.

2. Characterization of Zn(TFMA) oxocluster

i)FTIR of Zn(TFMA)

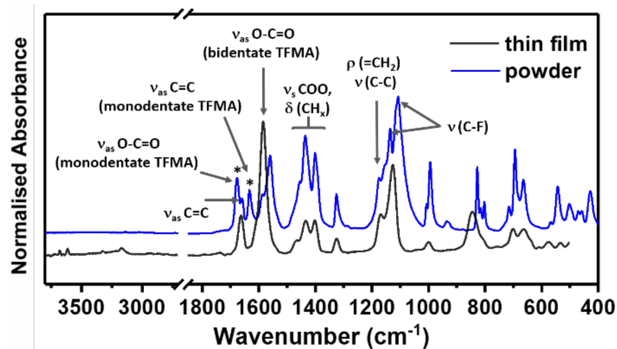

Figure S6.2: FTIR of synthesized Zn(TFMA) oxocluster: thin film and powder.

ii) Mass spectra of Zn(TFMA)

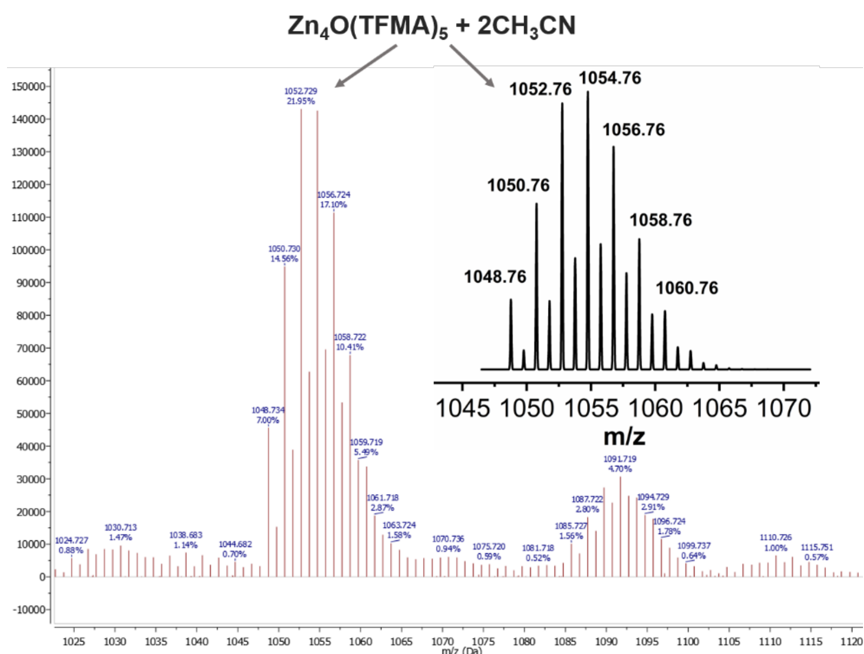

Figure S6.3: Mass spectra of Zn(TFMA) in acetonitrile using electronspray ionization (ESI). Simulated mass spectra using ChemCal is shown in black.

3. Scanning transmission X-ray microscope

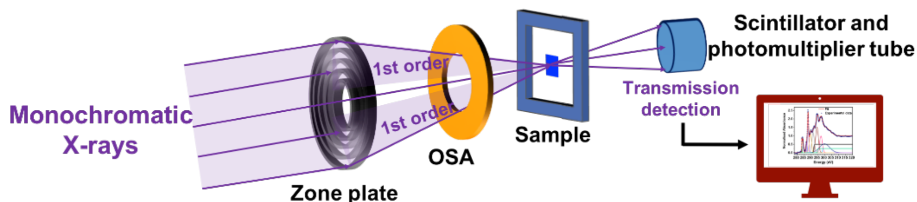

Figure S6.4: Schematic representation of STXM setup.

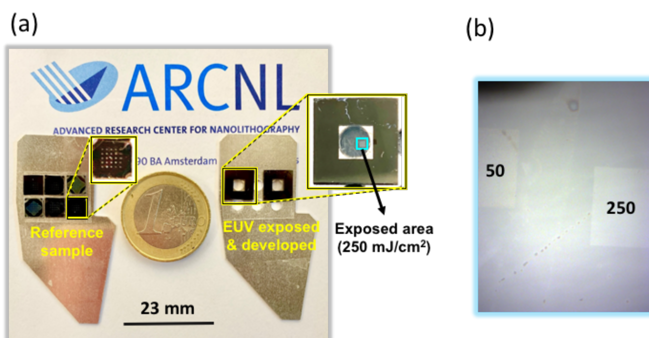

Figure S6.5: (a) Substrates attached to the sample holder; left sample holder represents the substrate used for reference samples and the right sample holder represents the sample exposed (EUV) and developed (propionic acid (0.1% in $CHCl_3$), and (b) optical image under AFM microscope of the resist exposed to EUV doses: 50 and 250 mJ/cm^2.

4. Stability study of the thin films of Zn(TFMA): UV-vis spectroscopy

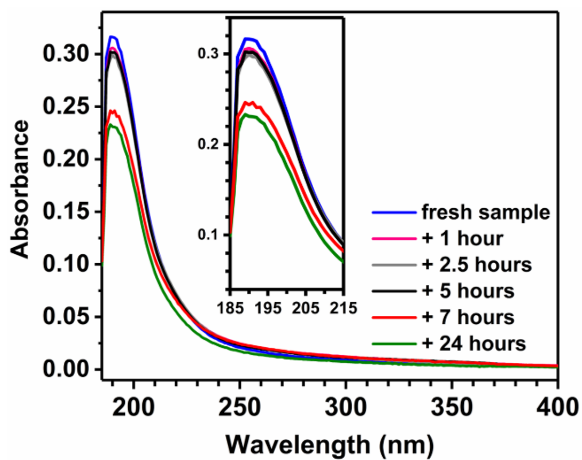

Figure S6.6: Monitoring changes in the absorption band to the ambient atmosphere of the double bond of TFMA ligand using UV-vis spectroscopy studies.

5. Silanization of the Si substrates:

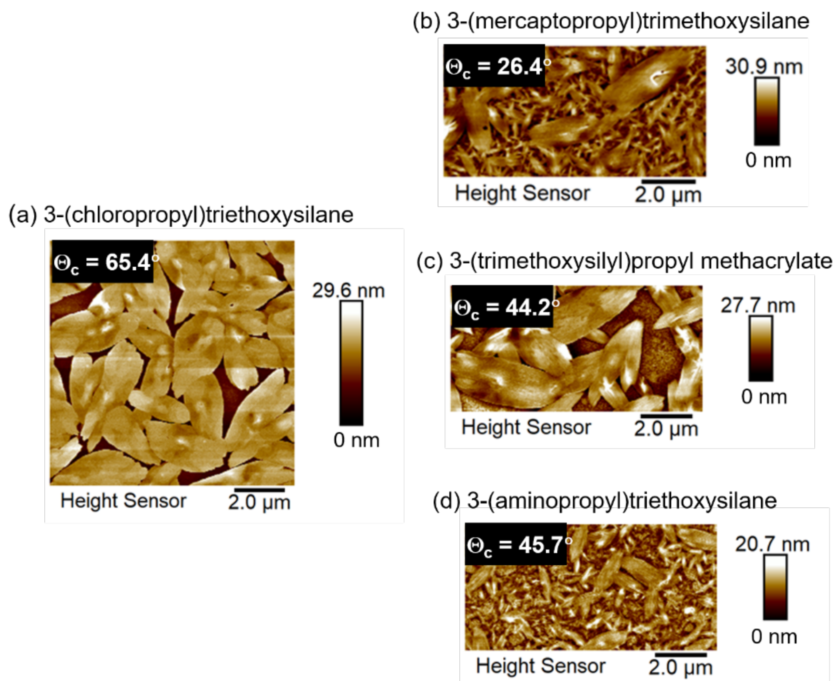

Figure S6.7: AFM images of the thin films of Zn(TFMA) spin coated on functionalized Si/SiO_2 surfaces. The water contact angles of the functionalized Si/SiO_2 substrate surface before spin coating are reported as Θ_c as insets in the AFM images.

6. Contrast curves for Zn(TFMA)(MA)(TFA) oxocluster

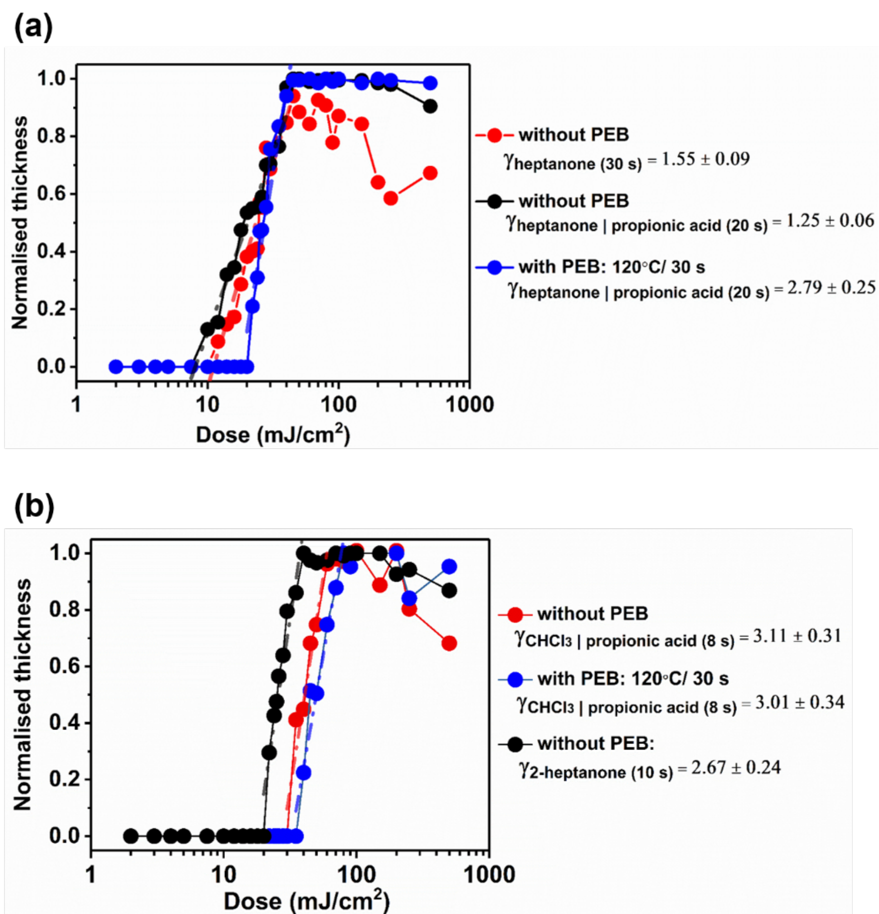

Figure S6.8: (a) Contrast curves for Zn(TFMA) thin films using acetonitrile as casting solvent and 2-heptanone or diluted propionic acid (0.1%) in 2-heptanone as developer, and (b) Contrast curves for Zn oxocluster, Zn(TFMA)(MA)(TFA) for thin films spin coated using casting solvent $CHCl_3$: PGMEA and developed using different solvents as mentioned in the labels. Development times are mentioned in the labels. The contrast values γ are the slopes of the curves between D_0 and ~D_{90} / ~D_{100}.

7. Spin coated thin films of oxoclusters

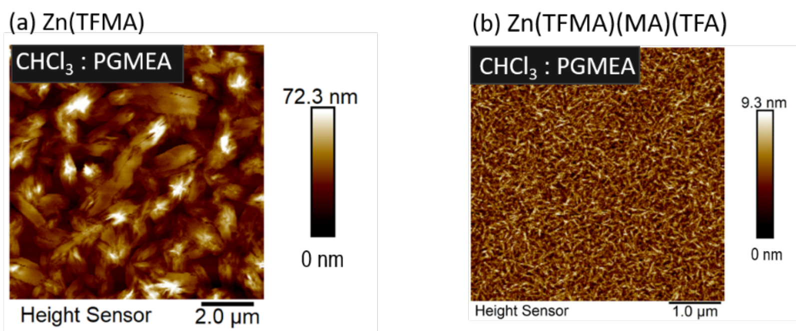

Figure S6.9: Thin film of Zn(TFMA) and Zn(TFMA)(MA)(TFA) spin coated on Si/SiO_2 substrate without any surface treatment.

8. SEM and AFM images of L/S features

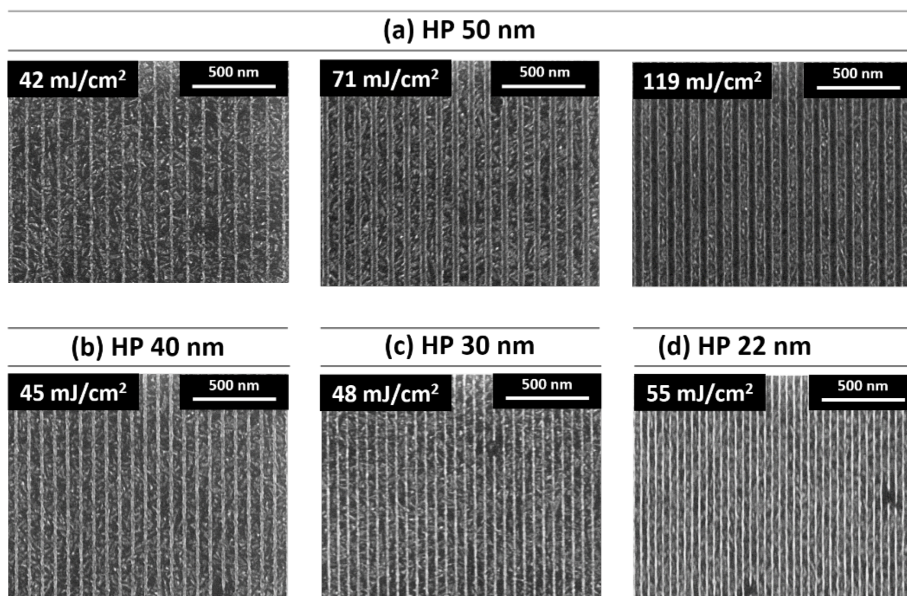

Figure S6.10: SEM top-down images of L/S patterns of different half pitch printed on Zn(TFMA)(MA)(TFA) oxocluster using 2-heptanone (10 s) as developer.

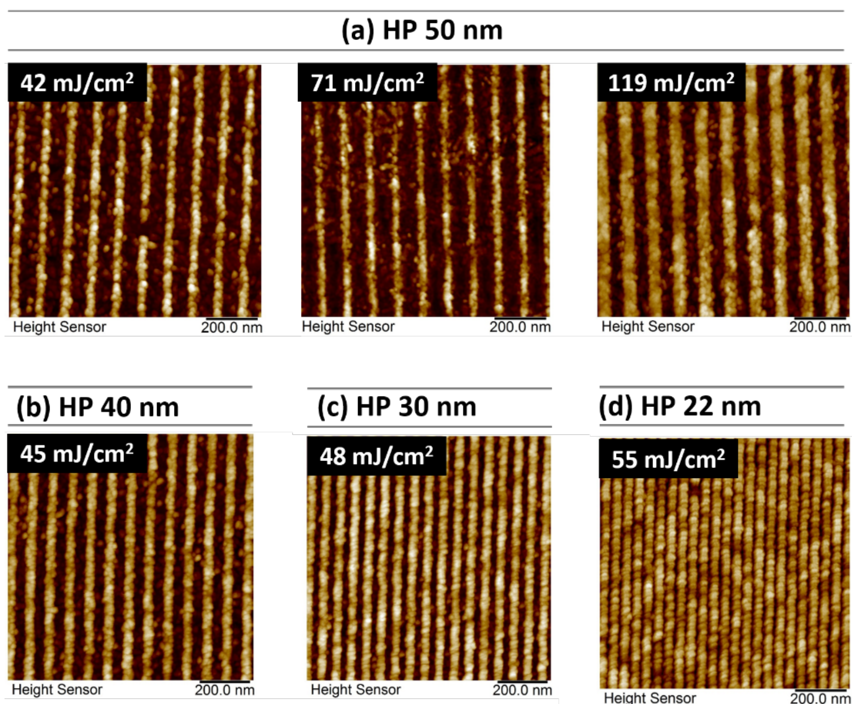

Figure S6.11: AFM images of L/S patterns of different half pitch printed on Zn(TFMA)(MA)(TFA) oxocluster using 2-heptanone (10 s) as developer.

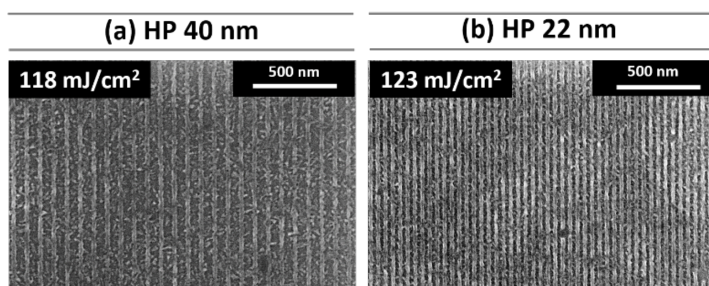

Figure S6.12: SEM images of L/S patterns of different half pitch printed on Zn(TFMA)(MA)(TFA) oxocluster using diluted propionic acid (0.05%) in $CHCl_3$ (8 s) as developer.

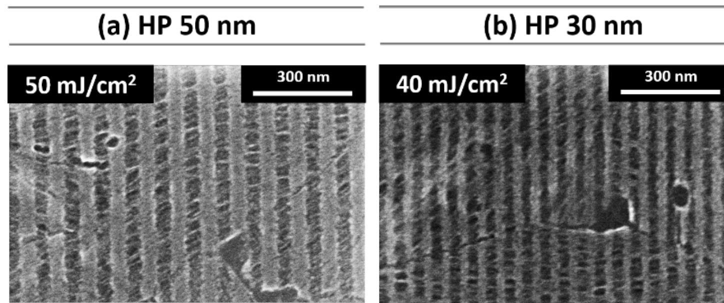

Figure S6.13: SEM images of L/S patterns printed on Zn(TFMA) oxocluster using 2-heptanone (25 s) as developer.

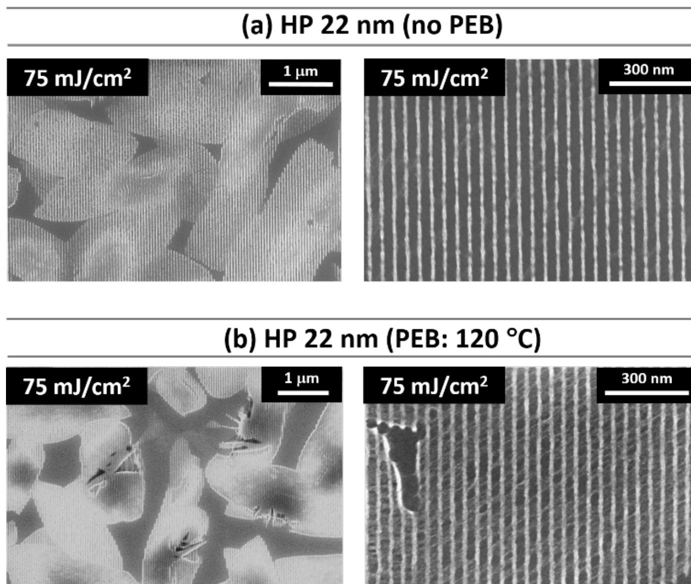

Figure S6.14: Figure S16: L/S features of half pitch 22 nm printed using EUV-IL on Zn(TFMA) photoresist thin film: (a) without PEB, and (b) applied PEB at 120 °C/30 s. Developed using diluted propionic acid (0.1%) in 2-heptanone (10 s).

9. STXM-XAS on Zn(TFMA) oxocluster thin films

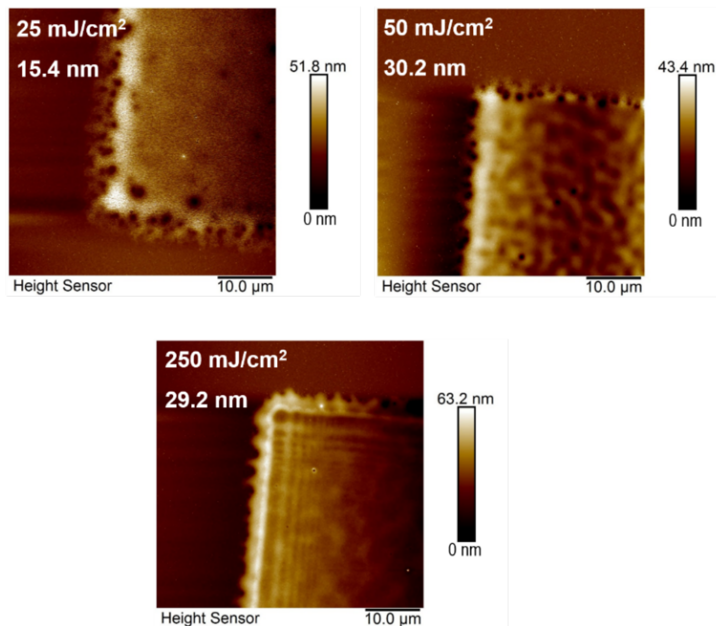

Figure S6.15: AFM images of the edge of EUV exposed area of Zn(TFMA) resist at different doses on SiN_x membrane. The average height difference between the exposed areas and the cleared background are reported in the figures.

(a) 25 mJ/cm²

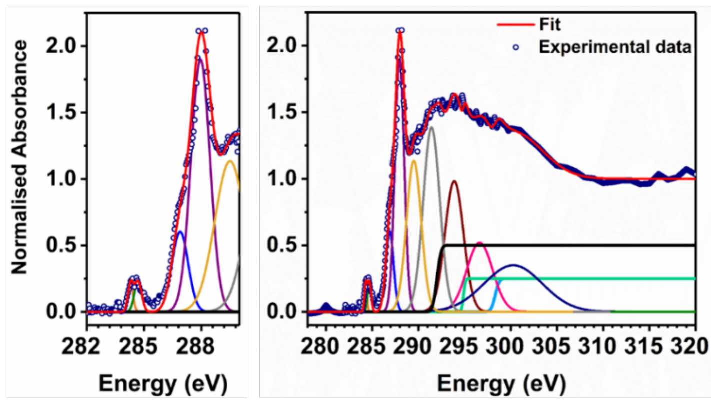

(b) 50 mJ/cm²

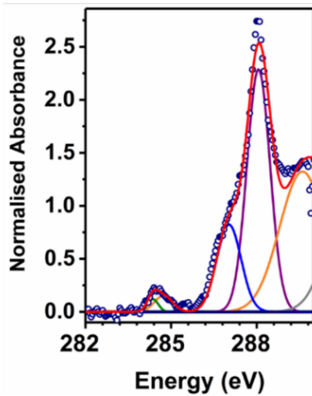

(c) 250 mJ/cm²

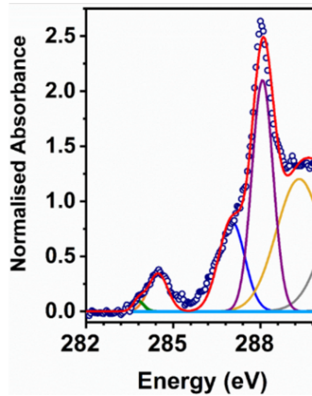

Figure S6.16: STXM-XAS C K-edge spectra of EUV exposed Zn(TFMA) thin film at different doses.

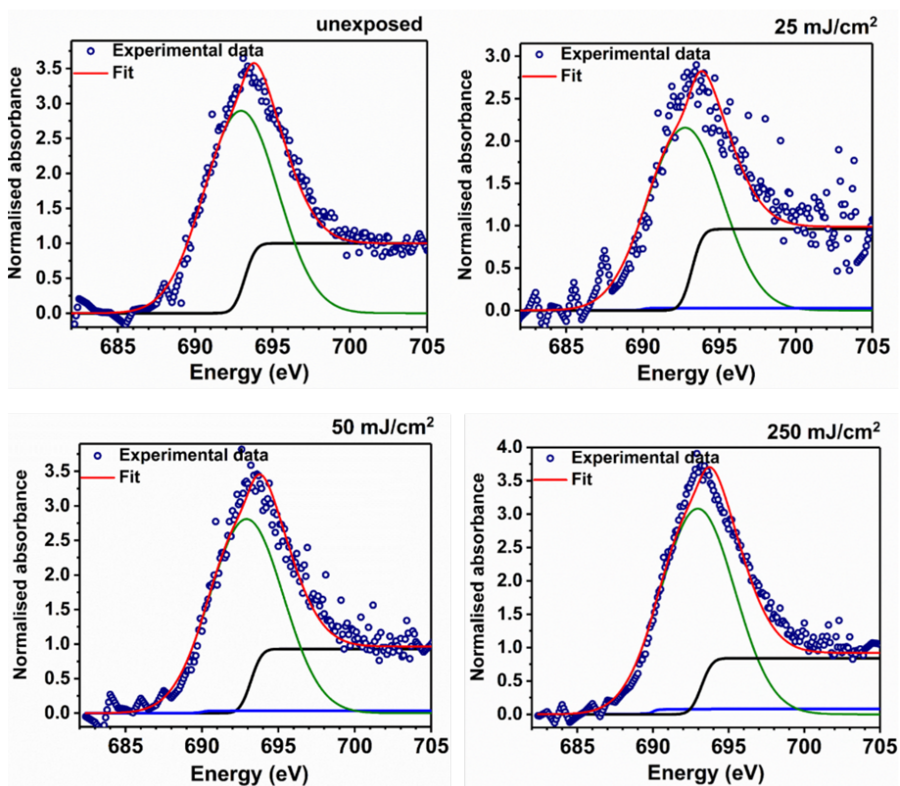

Figure S6.17: F K-edge XAS of Zn(TFMA) oxocluster exposed to different EUV doses.

Calculations of the lowest X-ray absorption transitions from the C(1*s*) orbitals were done using the Transition Potential (TP) method using AMS2021.[14,15] Trifluoromethacrylic acid and pivalic acid were used as model systems for the unexposed and polymerized materials. Structures were optimized with PBE-D4(EEQ)/TZP, without relativity corrections. For TP calculations we used the LDA functional and the QZ4P basis set. The low-energy regions of the predicted spectra and the lowest unoccupied MOs are shown in Figure S20. The calculations were also performed for the s-trans conformer of TFMA, which has a slightly higher energy than s-cis, but the results are very similar and are not shown here.

The two peaks at the lowest energy originate from transitions from C1*s* of C1 and C2 (see figure S20) to the delocalized LUMO. Experimentally, the energy difference between these two peaks is a bit smaller (284.2 eV and 284.7 eV). The third peak arises from transitions C1s (C1) to LUMO+1 (calculated at 272.9 eV) and C1*s* (C3) to LUMO (273.0 eV). The transition C1*s* (C2) to LUMO+1 is calculated at 273.7 eV. The latter three transitions are probably responsible for

the experimental peaks at 286.8 eV (shoulder) and 287.9 eV. In the model for the reaction product, the main peak arises from the transition from the C=O C1*s* to the LUMO, which is now the localized π* orbital of the C=O group.

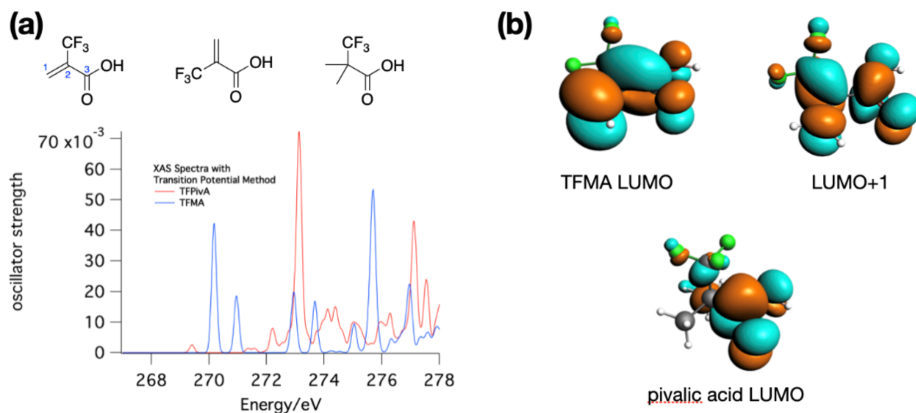

Figure S6.18: (a) Computed X-ray absorption spectra of TFMA and trifluoropivalic acid; (b) π* orbitals of TFMA and trifluoropivali**c** acid.

10. UV-vis spectroscopy:

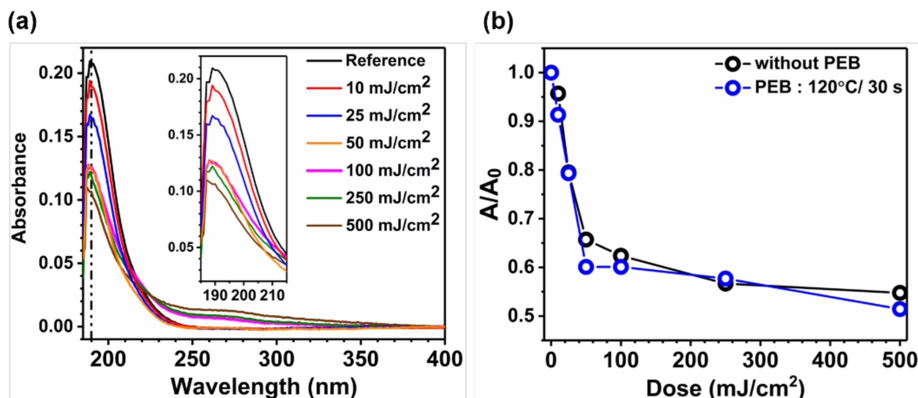

Figure S6.19: UV-vis spectroscopy on Zn(TFMA) sample (a) as a function of EUV dose with applied PEB at 120 °C/ 30 s and no development, and (b) A/A_0 at ~190 nm as a function of dose, where A represents the absorbance maxima here.

11. FTIR spectroscopy

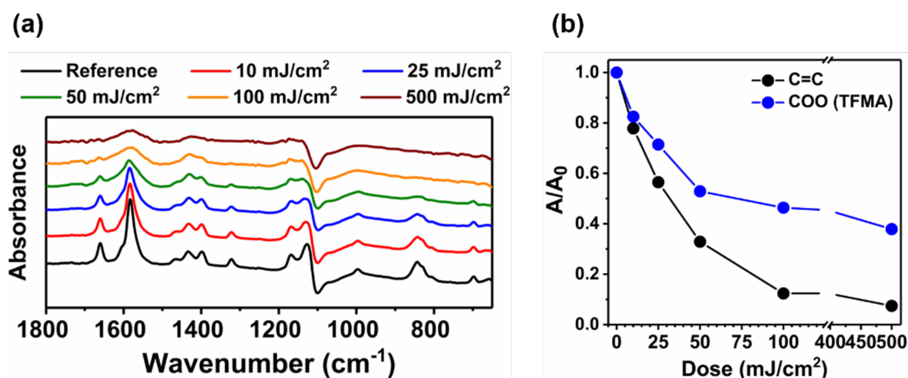

Figure S6.20: FTIR spectra of Zn(TFMA) sample (a) as a function of EUV dose with applied PEB at 120 °C/ 30 s and no development, and (b) A/A_0 as a function of dose of samples with applied PEB at 120 °C/ 30 s, where A represents the area under the peak.

12. XPS measurement

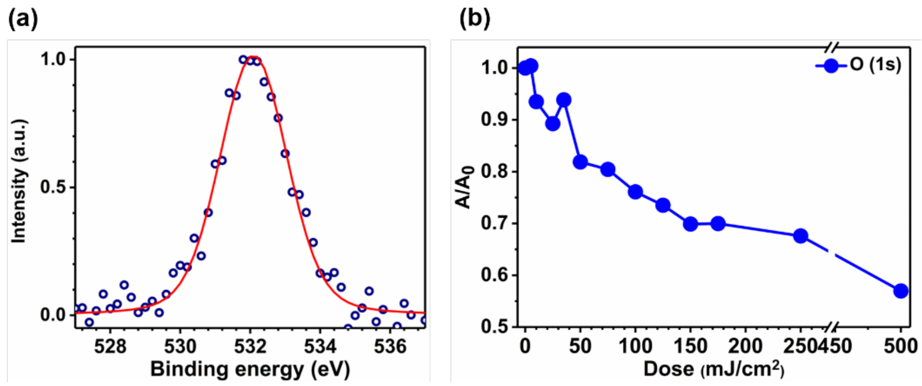

Figure S6.21: O (1*s*) XPS spectra of unexposed Zn(TFMA) thin film, and (b) A/A_0 as a function of EUV dose, where A represents the area under the peak.

References

[1] N. Thakur, L.-T. Tseng, M. Vockenhuber, Y. Ekinci, S. Castellanos, *J. Micro/Nanolithography, MEMS, MOEMS* **2019**, *18*, 043504.

[2] E. Polydorou, A. Zeniou, D. Tsikritzis, A. Soultati, I. Sakellis, S. Gardelis, T. A. Papadopoulos, J. Briscoe, L. C. Palilis, S. Kennou, *J. Mater. Chem. A* **2016**, *4*, 11844.

[3] T. Hamann, L. Kankate, E. Böhler, J. H. Bredehöft, F. M. Zhang, A. Gölzhäuser, P. Swiderek, *Langmuir* **2012**, *28*, 367.

[4] E. Böhler, J. H. Bredehöft, P. Swiderek, *J. Phys. Chem. C* **2014**, *118*, 6922.

[5] F. Schmidt, P. Swiderek, J. H. Bredehöft, *ACS Earth Sp. Chem.* **2019**, *3*, 1974.

[6] W. E. Wallace, "'Mass Spectra' in NIST Chemistry WebBook, NIST Standard Reference Database Number 69," DOI 10.18434/T4D303, (retrieved October 1, 2020)can be found under https://webbook.nist.gov/cgi/cbook.cgi?Contrib=MSDC**.**

[7] J. W. McConkey, C. P. Malone, P. V. Johnson, C. Winstead, V. McKoy, I. Kanik, *Phys. Rep.* **2008**, *466*, 1.

[8] V. Tarnovsky, K. Becker, *J. Chem. Phys.* **1993**, *98*, 7868.

[9] I. Torres, R. Martínez, F. Castaño, *J. Phys. B At. Mol. Opt. Phys.* **2002**, *35*, 2423.

[10] Y. K. Kim, K. K. Irikura, M. E. Rudd, M. A. Ali, P. M. Stone, J. Chang, J. S. Coursey, R. A. Dragoset, A. R. Kishore, K. J. Olsen, A. M. Sansonetti, G. G. Wiersma, D. S. Zucker, M. A. Zukker, "Electron-Impact Cross Sections for Ionization and Excitation Database, NIST Standard Reference Database 107," DOI 10.18434/T4KK5C, (accessed on March 19, 2021)can be found under https://www.nist.gov/pml/electron-impact-cross-sections-ionization-and-excitation-database, **2004**.

[11] K. O. Christe, D. Naumann, *Spectrochim. Acta Part A Mol. Spectrosc.* **1973**, *29*, 2017.

[12] J. Kreutzer, M. Puchberger, C. Artner, U. Schubert, *Eur. J. Inorg. Chem.* **2015**, *2015*, 2145.

[13] E. C. Mattson, Y. Cabrera, S. M. Rupich, Y. Wang, K. A. Oyekan, T. J. Mustard, M. D. Halls, H. A. Bechtel, M. C. Martin, Y. J. Chabal, *Chem. Mater.* **2018**, *30*, 6192.

[14] G. te Velde, F. M. Bickelhaupt, E. J. Baerends, C. F. Guerra, S. J. A. van Gisbergen, J. G. Snijders, T. Ziegler, *J. Comput. Chem.* **2001**, *22*, 931.

[15] L. Triguero, L. G. M. Pettersson, H. Ågren, *Phys. Rev. B* **1998**, *58*, 8097.